Statistical theory and applications of lock-in carrierographic image pixel brightness dependence on multi-crystalline Si solar cell efficiency and photovoltage

Andreas Mandelis,[1] Yu Zhang,[1,2] and Alexander Melnikov[1]
[1]*Center for Advanced Diffusion-Wave Technologies (CADIFT), Mechanical and Industrial Engineering, University of Toronto, Toronto, Ontario M5S 3G8, Canada*
[2]*Department of Automation Measurement and Control, Harbin Institute of Technology, Harbin 150001, China*

(Received 29 February 2012; accepted 9 August 2012; published online 7 September 2012)

A solar cell lock-in carrierographic image generation theory based on the concept of non-equilibrium radiation chemical potential was developed. An optoelectronic diode expression was derived linking the emitted radiative recombination photon flux (current density), the solar conversion efficiency, and the external load resistance via the closed- and/or open-circuit photovoltage. The expression was shown to be of a structure similar to the conventional electrical photovoltaic I-V equation, thereby allowing the carrierographic image to be used in a quantitative statistical pixel brightness distribution analysis with outcome being the non-contacting measurement of mean values of these important parameters averaged over the entire illuminated solar cell surface. This is the optoelectronic equivalent of the electrical (contacting) measurement method using an external resistor circuit and the outputs of the solar cell electrode grid, the latter acting as an averaging distribution network over the surface. The statistical theory was confirmed using multi-crystalline Si solar cells. © *2012 American Institute of Physics*. [http://dx.doi.org/10.1063/1.4749413]

I. INTRODUCTION

Modern solar cell industry has moved toward GW-scale production, with quality control becoming a critical factor.[1] Non-destructive and non-contacting methods for optoelectronic diagnostics of solar cells at all stages of the fabrication process are in strong demand. Several such methodologies have been developed for analyzing the excess charge carrier lifetime of Si wafers in a short time, including carrier density imaging.[2] Microwave photoconductance decay is a "golden standard" method for imaging lifetimes, including short recombination lifetimes, but it is more time-consuming.[3] Conventionally, the I-V characteristics are obtained by attaching a resistive load or a power source to the irradiated solar cell or using a flash tester[4] to measure and evaluate its efficiency. This practice requires electrical contacts to a solar cell and is thus not well suited for mass production. Photoluminescence imaging (PL) is a fast non-destructive and non-contacting camera based diagnostic method which has been used for detecting electronic and other defects associated with crystal imperfections and handling of solar cells.[5–8] However, dc PL cannot monitor the optoelectronic carrier kinetics of surface and near-subsurface regions due to its depth-integrated character through the signal dependence on the dc carrier diffusion length.[8] Laser-induced infrared photocarrier radiometry (PCR)[9] is a dynamic near-infrared (NIR) modulated PL, spectrally gated to filter out the thermal infrared component of the radiative emission spectrum from de-exciting free photocarriers. This emission is governed by the Law of Detailed Balance on which the non-equilibrium kinetics of optoelectronic device operation is based.[10] The infrared spectral complement of PCR concerns Planck (blackbody) thermal emissions due to nonradiative carrier de-excitations and can be detected using photothermal radiometry (PTR), a modulated thermal-wave generation and detection method.[11] The imaging equivalent of PTR is lock-in thermography which has also been used to investigate local power losses in solar cells.[12–14] PCR has proven to be an effective non-contact methodology for the measurement of transport properties in semiconductors.[9,15] Lock-in carrierography (LIC) is a dynamic NIR InGaAs-camera-based photocarrier radiometric PL imaging method recently introduced as an imaging extension of PCR.[16] LIC is further developed in this paper theoretically and experimentally to obtain relationships between surface-averaged distributions of optoelectronic energy conversion efficiencies and output photovoltages of entire Si solar cells on one hand, and radiative recombination modulated emission images on the other. In this manner, the solar efficiency and photovoltage can be measured without the need for contacting electrodes. The essence of quantitative carrierography (CG) as a non-equilibrium excess photocarrier PL imaging technique lies in the treatment of radiative emission fluxes from semiconductors as representative of the non-equilibrium carrier densities that generated them. This is entirely analogous to the Planck (blackbody) equivalent[9] and is expressed by the non-equilibrium physics of the generalized Planck law of radiation for non-black bodies.[17] The inherent dependence of the imaging contrast on the free photocarrier density depth integral[9] is the modulated carrier diffusion-wave equivalent to modulated thermal waves on which thermography is based and has provided the motivation for naming this dynamic PL imaging technique "carrierography."[16]

In this paper, we develop the theory of the optoelectronic analog of the conventional photovoltaic diode equation and its application to the noncontact determination of solar conversion efficiency and photovoltage of industrial Si solar cells by means of modulated carrierographic imaging.

 © 2012 American Institute of Physics

Downloaded 24 Sep 2013 to 128.100.48.8. This article is copyrighted as indicated in the abstract. Reuse of AIP content is subject to the terms at: http://jap.aip.org/about/rights_and_permissions

II. THEORY OF QUANTITATIVE SOLAR CELL CARRIEROGRAPHIC IMAGING

Würfel[17] and Würfel *et al.*[18] have discussed non-equilibrium radiative electronic recombination transitions associated with non-thermal infrared photon emissions in semiconductors, in terms of a radiation chemical potential μ_γ. The essence of their theory was to link these non-equilibrium optical (non-thermal luminescence) phenomena to their limiting (equilibrium) case $\mu_\gamma = 0$ in the framework of a thermodynamic treatment of radiation involving the generalization of Planck's radiation law for luminescence. Würfel's theory adapted to the case of the excitation of a solar cell *p-n* junction by an incident superband-gap photon flux of energy $E_i = \hbar\omega_i$ yields a relationship between the photovoltage appearing across the junction and the chemical potential of electron-hole pairs

$$qV_{\hbar\omega} = \mu_e + \mu_h = \mu_\gamma, \tag{1}$$

where q is the elementary charge. Here, μ_e, μ_h are the electron and hole quasi-Fermi levels. The Stokes-shifted (PCR) photon flux ($\mathrm{cm}^{-2}\,\mathrm{s}^{-1}$) emitted with infrared energy $E = \hbar\omega$ in response to the incident photon excitation and absorption is given by[17]

$$F_R(\hbar\omega; V_{\hbar\omega}, T) = \frac{A(\hbar\omega)}{4\pi^2\hbar^3c^2}\left\{\frac{(\hbar\omega)^3}{\exp[(\hbar\omega - qV_{\hbar\omega})/kT] - 1}\right\}, \tag{2}$$

where A is the absorptivity of the non-blackbody emitter of non-thermal radiation at energy $\hbar\omega$ and c is the speed of light in the medium ($=c_0/n_r$; n_r: medium refractive index). For indirect gap semiconductors like Si, the chemical potential μ_γ also includes the energy of either an emitted or an absorbed phonon acting as a mediator of the indirect band-to-band electronic transition.[18] This extra term can be incorporated in the (shifted, effective) value of $\hbar\omega$ in Eq. (2), which essentially leaves the form of the equation unchanged. For semiconductor materials of bandgap energy $E_G > 1\,\mathrm{eV}$, the exponent of the denominator gives $\hbar\omega - qV_{\hbar\omega} \gg kT$, so that the emitted flux can be accurately approximated as

$$F_R(\hbar\omega; V_{\hbar\omega}, T) \cong \left[\left(\frac{A(\hbar\omega)(\hbar\omega)^3}{4\pi^2\hbar^3c^2}\right)e^{-\hbar\omega/kT}\right]\exp\left(\frac{qV_{\hbar\omega}}{kT}\right). \tag{3}$$

In Eq. (2) setting $V_{\hbar\omega} = 0$ results in the well-known equilibrium black-body Planck emission equation, the limit of zero chemical potential μ_γ.

Non-radiative processes affect the excess photoexcited carrier density available for radiative recombination in dc-excitation processes, and the carrier density wave in ac-processes resulting from optical power modulation. The effect involves phonon emission and absorption processes with energies $E_{NR} = \hbar\omega_{NR}$, especially important in indirect semiconductors like Si.[18] It is manifested as decreased photovoltage $V_{\hbar\omega} = \mu_\gamma$, which also decreases the PCR photon flux. The total flux is

$$F_T(V_{\hbar\omega}, T) = \eta_R(T)F_R(\hbar\omega; V_{\hbar\omega}, T) + \eta_{NR}F_{NR}(\hbar\omega_{NR}, T), \tag{4}$$

where η_R and η_{NR} are the radiative and non-radiative (quantum) efficiencies, respectively. Here, F_{NR} is the heat flux resulting from the non-radiative conversion of optoelectronic to thermal energy. These efficiencies can be expressed in terms of radiative and non-radiative recombination probabilities,[19]

$$\eta_R(T) = \frac{P_R(T)}{P_R(T) + P_{NR}(T)}, \quad \eta_{NR}(T) = \frac{P_{NR}(T)}{P_R(T) + P_{NR}(T)}, \tag{5}$$

provided no other energy conversion pathways exist. For solar or other optical superband-gap illumination, η_R becomes a function of the generated photovoltage

$$\eta_R(T) = \frac{F_R(\hbar\omega, T) - F_R(0, T)}{F_A(\hbar\omega_i)} = \frac{F_R(0, T)}{F_A(\hbar\omega_i)}\left[\exp\left(\frac{qV_{\hbar\omega}}{kT}\right) - 1\right]. \tag{6}$$

Here, F_A is the absorbed flux of incident photons and $F_R(0, T)$ is the background (residual) equilibrium flux (in the dark), given by Eq. (3) with $V_{\hbar\omega} = 0$. Under equilibrium conditions, Kirchhoff's law applies and the residual radiative emission becomes thermal. The emission rate is then equal to the absorption rate. Equation (6) can be written in terms of the photon flux incident on the solar cell and the non-radiative recombination (thermal generation) flux can be added to the overall photon conversion. Simplifying the notation

$$F_A(\hbar\omega_i) = \frac{1}{\eta_R}[F_R(V_{\hbar\omega}) - F_R(0)] + \eta_{NR}F_{NR}. \tag{7}$$

This equation is valid under open-circuit conditions, assuming that both radiative and non-radiative recombinations can occur. Under closed-circuit conditions (the most general case), an optical-to-photocurrent energy conversion pathway must be added which gives rise to a photocurrent flux, F_C, on the rhs of Eq. (7)

$$F_A(\hbar\omega_i) = \frac{1}{\eta_R}[F_R(V_{\hbar\omega}) - F_R(0)] + \eta_{NR}F_{NR} + F_C. \tag{8}$$

Now, we define the following current densities (charge fluxes, $\mathrm{A/m}^2$):

$$\begin{aligned} J(V_{\hbar\omega}) &\equiv qF_C(V_{\hbar\omega}),\\ J_{SC}(\hbar\omega_i) &\equiv qF_A(\hbar\omega_i),\\ J_0(\hbar\omega) &\equiv \frac{1}{\eta_R}[qF_R(0)] = \frac{1}{\eta_R}\left[\frac{qA(\hbar\omega)(\hbar\omega)^3}{4\pi^2\hbar^3c^2}\right]\exp\left(-\frac{\hbar\omega}{kT}\right),\\ J_{NR} &\equiv \eta_{NR}qF_{NR}. \end{aligned} \tag{9}$$

Downloaded 24 Sep 2013 to 128.100.48.8. This article is copyrighted as indicated in the abstract. Reuse of AIP content is subject to the terms at: http://jap.aip.org/about/rights_and_permissions

Rearranging Eq. (8) while taking Eq. (6) into account and introducing definitions (9) results in

$$J(V_{\hbar\omega}) = J_{SC}(\hbar\omega_i) - J_0(\hbar\omega)\left[\exp\left(\frac{qV_{\hbar\omega}}{kT}\right) - 1\right] - J_{NR}. \tag{10}$$

This equation can now be compared to the solar cell diode equation without series resistance and ideality factor n

$$J(V) = J_{SC} - J_0\left[\exp\left(\frac{qV}{nkT}\right) - 1\right] - (V/SR_{sh}), \tag{11}$$

where S is the illuminated surface area of the solar cell and R_{sh} is the shunt resistance. The comparison reveals that the radiative diode equation (10) involves unity ideality factor and a reverse optical flux (saturation current density-equivalent factor) J_0 given in Eq. (9). J_0 depends on $F_R(0)/\eta_R$, where $F_R(0)$ is the equilibrium blackbody flux radiated by the solar cell (and equally absorbed at equilibrium) in the dark and η_R includes the non-equilibrium (non-thermal) radiation processes, Eq. (6). Higher radiative efficiencies produce less optical saturation current, as expected. Similarly, $\eta_{NR}F_{NR}$ is the thermal current flux and produces effects similar to the electrical shunt resistance: $\eta_{NR}F_{NR} = 0$ corresponds to $R_{sh} \to \infty$, i.e., there are no losses (thermal emissive or electrical, respectively). Despite their formal similarity, the important difference between Eqs. (10) and (11) is that the latter connects purely electrical quantities: the measurable current density, J, flowing out of the solar cell as a function of the photovoltage, V, across the junction, whereas the former links an optically measurable quantity, the non-equilibrium radiative flux $J_0(\hbar\omega)\exp(qV_{\hbar\omega}/kT)$, to the electrical current density. Therefore, the importance of Eq. (10) lies in the fact that it provides a linkage between fully non-contacting, remote photocarrier radiometric measurements of radiative emission rates (like dc PL, modulated PCR signals, and carrierographic images) and solar cell electrical parameters which otherwise require contacting electrical measurements and the presence of electrode grids.

As a byproduct of the formal similarity between Eqs. (10) and (11), a number of expressions can be derived from Eq. (10) between radiative fluxes, current densities, and photovoltages by using well-known electrical relations for solar cells stemming from Eq. (11). The relevant quantities are the open-circuit photovoltage

$$V_{\hbar\omega}^{OC} = V_{\hbar\omega}(J=0) = \left(\frac{kT}{q}\right)\ln\left(1 + \frac{\Delta J}{J_0}\right) \cong \left(\frac{kT}{q}\right)\ln\left(\frac{\Delta J}{J_0}\right), \tag{12a}$$

where $\Delta J \equiv J_{SC} - J_{NR}$ (for conventional solar cells $J_0 \ll \Delta J$) and the closed-circuit photovoltage

$$V_{\hbar\omega}(J) = \left(\frac{kT}{q}\right)\ln\left(1 + \frac{\Delta J}{J_0} - \frac{J}{J_0}\right) \cong \left(\frac{kT}{q}\right)\ln\left(\frac{\Delta J - J}{J_0}\right). \tag{12b}$$

The output photovoltaic power density is $P_{\hbar\omega} = JV_{\hbar\omega}$. Maximizing the power density with respect to photovoltage, $\frac{\partial P_{\hbar\omega}}{\partial V_{\hbar\omega}} = 0$, yields the optical equivalent of the well-known transcendental equation for the photovoltage, $V_{\hbar\omega}^{mp}$, at maximum output power

$$\exp\left(\frac{qV_{\hbar\omega}^{mp}}{kT}\right)\left[1 + \left(\frac{qV_{\hbar\omega}^{mp}}{kT}\right)\right] = 1 + \frac{\Delta J}{J_0} = \exp\left(\frac{qV_{\hbar\omega}^{OC}}{kT}\right), \tag{13}$$

which, when combined with the expression

$$J_{mp} \equiv J(V_{\hbar\omega}^{mp}) = \Delta J - J_0\left[\exp\left(\frac{qV_{\hbar\omega}^{mp}}{kT}\right) - 1\right] \tag{14}$$

obtained from Eq. (10), results in the following expression for the maximum power density:

$$P_{\max} = J_{mp}V_{\hbar\omega}^{mp} = \frac{(qV_{\hbar\omega}^{mp}/kT)V_{\hbar\omega}^{mp}\Delta J}{1 + (qV_{\hbar\omega}^{mp}/kT)}\left(1 + \frac{J_0}{\Delta J}\right). \tag{15}$$

The maximum solar conversion efficiency is given by

$$\eta_{\max} = \left[\frac{(qV_{\hbar\omega}^{mp}/kT)}{1 + (qV_{\hbar\omega}^{mp}/kT)}\right]\frac{V_{\hbar\omega}^{mp}\Delta J}{P_i}, \tag{16}$$

where P_i is the incident superband-gap optical or solar power density (W/m^2). With $qV_{\hbar\omega}^{mp} \sim 0.5$–$0.6$ eV for Si solar cells[19] and room-temperature $kT = 0.026$ eV, Eq. (16) can be simplified

$$\eta_{\max} = \frac{V_{\hbar\omega}^{mp}\Delta J}{P_i} \cong \frac{V^{OC}\Delta J[FF]}{P_i}. \tag{16a}$$

An expression for the fill factor (FF) has been provided by Ghosh *et al.*[20]

$$FF \cong \left[1 - \frac{1}{\ln(J_{SC}/J_0)}\right]\left[1 - \frac{\ln[\ln(J_{SC}/J_0)]}{\ln(J_{SC}/J_0)}\right] \approx 1 - \frac{1}{\ln(J_{SC}/J_0)}. \tag{17}$$

Therefore, from Eq. (12a), to first order with $J_{SC} \gg J_0$

$$\eta_{\max} = \left(\frac{nkT}{q}\right)\frac{\Delta J}{P_i}[\ln(\Delta J) + \ln(J_0)]. \tag{18}$$

This equation indicates that for an ideal solar cell, there is a logarithmic decrease of solar conversion efficiency with reverse radiative saturation current. Its electronic counterpart has been confirmed by Fahrenbruch and Bube (Ref. 19, p. 216, Fig. 6.5) for a wide range of non-ideality factors. When using the optoelectronic Eq. (10) instead of the conventional Eq. (11), the solar conversion efficiency is given by

$$\eta_{\max} = \left(\frac{nkT}{q}\right)\frac{\Delta J}{P_i}\left[\ln\left(\frac{\Delta J}{qF_R(0)}\right) + \ln(\eta_R)\right]. \tag{19}$$

Here, a non-ideality factor n was added *ad hoc*, in order to account for physical PCR and carrierographic responses of the *p-n* junction. In the framework of the chemical potential formalism of non-thermal radiation,[17] η_{max} plays the role of the maximum chemical potential $\mu_{\gamma,max}$ (quasi-Fermi level difference) of the radiative emission by recombining free

Downloaded 24 Sep 2013 to 128.100.48.8. This article is copyrighted as indicated in the abstract. Reuse of AIP content is subject to the terms at: http://jap.aip.org/about/rights_and_permissions

electron-hole photocarriers. From the definition of η_R, Eq. (6)

$$\eta_R(T) = \frac{F_R(\hbar\omega,T) - F_R(0,T)}{F_A(\hbar\omega_i)} = \frac{J_R(V_{\hbar\omega}) - J_R(0)}{J_{SC}} \equiv \frac{J_{PCR}(V_{\hbar\omega})}{J_{SC}}, \tag{20}$$

where $J_R(V_{\hbar\omega}) \equiv qF_R(V_{\hbar\omega})$. $J_{PCR}(V_{\hbar\omega}) \equiv q[F_R(V_{\hbar\omega}) - F_R(0)]$ is the photocarrier radiometric photon (luminescence) current density, a non-equilibrium quantity which can also be used for the definition of radiative non-thermal emission rates that generate carrierographic imaging. The radiatively recombining carriers are generated by the absorbed photon flux F_A, and their density is limited by competing non-radiative and external electrical current generation processes. For photocarrier excitation modulated at angular frequency ω_M, leading, e.g., to PCR signals from a laser spot illumination and single photodetector element detection, or to ac carrierographic (LIC) imaging (broad surface excitation and camera detection), the emitted non-thermal optical current density identified as $J_{PCR}(V_{\hbar\omega})$ is proportional to the depth integral of the excess photogenerated carrier density $\Delta N(z,\omega)$[18] over the wafer thickness L, generalized for the physics of non-linear radiative recombination processes[21] with non-linearity coefficient ν

$$J_{PCR}(V_{\hbar\omega};\omega_M) = K\int_0^L \Delta N^{\nu}(z,\omega_M)dz = CS_{CG}(\omega_M). \tag{21}$$

Here, K and C are constants independent of the photocarrier depth profile (see Sec. IV). Equation (21) shows that the same PCR depth integral is responsible for the carrierographic signal, $S_{CG}(\omega_M)$, as captured by a near-infrared camera. From Eqs. (19)–(21), the following expression is obtained for the maximum solar conversion efficiency:

$$\eta_{\max} = \left(\frac{nkT}{q}\right)\frac{\Delta J}{P_i}\left[\ln\left(\frac{\Delta J}{qF_R(0)}\right) + \ln[CS_{CG}(\omega_M)]\right]. \tag{22}$$

This expression predicts a logarithmic relationship between the local carrierographic signal and the measured solar conversion efficiency. It should be noted that for signals at angular modulation frequency ω_M, such as PCR and LIC imaging, complex quantities ΔJ, P_i, and $S_{CG}(\omega_M)$ are implied in Eq. (22). The general form of these quantities is $Z(\omega_M) = |Z(\omega_M)|e^{i\phi(\omega_M)}e^{i\omega_M t}$ and Eq. (22) remains valid in its complex version, provided an amplitude expression $|Z|$ is substituted for each complex quantity Z.

Equation (22) can be used for quantitative measurements of CG images of optoelectronically inhomogeneous solar cells with respect to local maximum radiative recombination efficiency. Introducing mean-value definitions over the illuminated surface, S, of a solar cell

$$\langle\eta\rangle = \frac{1}{S}\int\int_{x,y}\eta_{\max}(x,y)dxdy,$$
$$\langle S_{CG}(\omega_M)\rangle = \frac{1}{S}\int\int_{x,y}S_{CG}(x,y;\omega_M)dxdy, \tag{23}$$

and using an approximation based on the slower change of spatially variable logarithmic functions compared to linear functions, one obtains

$$\left\langle \Delta J\ln\left(\frac{\Delta J}{qF_R(0)}\right)\right\rangle = \frac{1}{S}\int\int_{x,y}\Delta J(x,y)\ln\left[\frac{\Delta J(x,y)}{qF_R(0)}\right]dxdy \cong \frac{1}{S}\left\langle \ln\left[\frac{\Delta J(x,y)}{qF_R(0)}\right]\right\rangle\int\int_{x,y}\Delta J(x,y)dxdy = \langle\Delta J\rangle\left\langle \ln\left[\frac{\Delta J(x,y)}{qF_R(0)}\right]\right\rangle. \tag{24}$$

Similarly, the expression

$$\langle\Delta J\ln[CS_{CG}(\omega_M)]\rangle \cong \langle\Delta J\rangle\langle\ln[CS_{CG}(\omega_M)]\rangle \tag{25}$$

can be adopted by means of the same approximation, and Eq. (22) can be rearranged and written in a mean-value form, averaged over the extent of the illuminated solar cell surface

$$\langle\ln[CS_{CG}(\omega_M)]\rangle = \left(\frac{qP_i}{nkT\Delta J}\right)\langle\eta_{\max}(\omega_M)\rangle - \left\langle\ln\left[\frac{\Delta J}{qF_R(0)}\right]\right\rangle. \tag{26}$$

This equation assumes a constant flux of optical illumination power over the illuminated surface of the solar cell. It also assumes that each pixel of the recombination-radiation-capturing camera receives a photon flux at the maximum local chemical potential, i.e., at $V_{\hbar\omega}^{OC}$. This is the case with the CG response of a solar cell irradiated at open circuit or even during the fabrication process, before electrodes are attached to it. Owing to the spatially strong damped subsurface distribution of the carrier diffusion wave, a function of ω_M, the mean value $\langle\eta\rangle$ will depend on ω_M as indicated in Eq. (26), because integration over the wafer thickness, Eq. (21), will yield different depth distributions of local radiative recombination efficiencies at different modulation frequencies in strongly electronically depth-inhomogeneous devices like solar cells, on account of the frequency-dependent ac (complex) carrier diffusion length[22]

$$L_e(\omega_M) = \sqrt{\frac{D^*\tau}{1+i\omega_M\tau}}. \tag{27}$$

Here, D^* is the ambipolar carrier diffusivity and τ is the minority recombination lifetime of the carrier diffusion wave. This implies that CG images of the same device obtained at different modulation frequencies will generally be different, the result of contrast variations generated by the local values of $\eta_R(x,y,z)$ radiative recombination efficiency.

Now, turning to the complex nature of the rhs of Eq. (22), one may write

$$CS_{CG}(\omega_M) = |CS_{CG}(\omega_M)|\exp[i\phi_{CG}(\omega_M)],$$
$$\Delta J(\omega_M) = |\Delta J(\omega_M)|\exp[i\phi_{\Delta J}(\omega_M)], \tag{28}$$
$$P_i = |P_i|,$$

Downloaded 24 Sep 2013 to 128.100.48.8. This article is copyrighted as indicated in the abstract. Reuse of AIP content is subject to the terms at: http://jap.aip.org/about/rights_and_permissions

where the common time modulation factor $e^{i\omega_M t}$ has been omitted for simplicity. Rearrangement of Eq. (22) with P_i transferred to the lhs, and separation of real and imaginary parts yields the following relation between the CG phase and the maximum solar conversion efficiency:

$$\phi_{CG}(\omega_M) = -\left(\frac{q|P_i|\sin(\phi_{\Delta J})}{kT|\Delta J(\omega_M)|}\right)\eta_{\max}(\omega_M) - \phi_{\Delta J}(\omega_M). \quad (29)$$

This relation can be extended to the mean-value (average) of the phase over the illuminated surface area in a manner and approximations similar to those used in the derivation of Eq. (26)

$$\langle\phi_{CG}(\omega_M)\rangle = -\left\langle\left(\frac{q|P_i|\sin(\phi_{\Delta J})}{kT|\Delta J(\omega_M)|}\right)\right\rangle\langle\eta_{\max}(\omega_M)\rangle - \langle\phi_{\Delta J}(\omega_M)\rangle. \quad (30)$$

The foregoing theory can also be used to predict the dependence of the carrierographic amplitude on photovoltage. From the definition of $V_{\hbar\omega}$, Eq. (12b), with J_0 from Eq. (9) and $J_{PCR}(V_{\hbar\omega}) \equiv q[F_R(V_{\hbar\omega}) - F_R(0)]$, the following expression can be derived:

$$V_{\hbar\omega} = \left(\frac{nkT}{q}\right)\frac{\Delta J}{P_i}\left[\ln\left(\frac{\Delta J - J}{qF_R(0)}\right) + \ln[CS_{CG}(\omega_M)]\right], \quad (31)$$

which also yields

$$V_{\hbar\omega}^{OC} = \left(\frac{nkT}{q}\right)\frac{\Delta J}{P_i}\left[\ln\left(\frac{\Delta J}{qF_R(0)}\right) + \ln[CS_{CG}(\omega_M)]\right]. \quad (32)$$

A relationship between the dc photovoltage, V, and the excess minority carrier density has been presented by Trupke *et al.*[23] in the form

$$qV = \Delta\eta \approx kT\ln\left(\frac{\Delta N(\Delta N + N_D)}{n_i^2}\right) \approx kT\ln(I_{PL}) + C. \quad (33)$$

Here, $\Delta\eta$ is the separation of the quasi Fermi energies, N_D is the doping density, ΔN is the excess minority carrier concentration, n_i is the equilibrium carrier density, and I_{PL} is dc photoluminescence intensity. Equation (33) bears a similarity to Eq. (31) in terms of the functional dependence between excess carrier density-dependent quantities and photovoltage, but it does not account for depth inhomogeneity or for the depth-integrated nature of radiative emission efficiencies, nor does it specify what constitutes the empirical constant C. The derivation of Eq. (33) assumed $\Delta\eta$ to be constant along the width of the solar cell base. The mean-value form of Eq. (31), averaged over the extent of the illuminated solar cell surface is

$$\langle V_{\hbar\omega}(\omega_M)\rangle \cong \left(\frac{nkT}{q}\right)\frac{\langle\Delta J\rangle}{P_i} \times\left[\left\langle\ln\left(\frac{\Delta J - J}{qF_R(0)}\right)\right\rangle + \langle\ln[CS_{CG}(\omega_M)]\rangle\right]. \quad (34)$$

The corresponding expression for $\langle V_{\hbar\omega}^{OC}(\omega_M)\rangle$ with $J = 0$ can be readily derived from Eq. (34).

III. MATERIALS AND EXPERIMENT SET-UP

Ten industrial multicrystalline solar cells (156×156 mm^2 area, 0.2 mm thickness) from Enfoton Solar Ltd., Cyprus, were used for LIC measurements. Subsequently, one solar cell was selected and sequentially damaged through gentle front-surface rubbing with fine sandpaper. Imaging measurements were made before and after each procedure. The schematic of the LIC experiment set-up is shown in Fig. 1. A near infrared camera (SU320KTSW-1.7RT/RS170 from Goodrich Sensors Unlimited) with a long-pass filter was used. The camera has a 320×256 pixel active element, spectral bandwidth 0.9-1.7 μm, frame rate 119.6 Hz for window size corresponding to the full 320×256 pixels, and full-frame exposure times ranging from 0.13 ms to 16.6 ms. A PCI-1427 frame grabber from National Instruments was used to read the camera image by a computer and to produce computer-generated amplitude and phase images using homemade software. Optical illumination was performed with two fiber coupled 9-W 808-nm infrared diode lasers with stability better than 1% at maximum output power. The two lasers were used so as to attain sufficient optical flux over the full surface of our solar cells. The laser beams were spread and homogenized by engineered microlens arrays forming a square illumination area with uniform intensity around 0.04 W/cm^2. A data acquisition module USB 6259 (from National Instruments) was used to generate sinusoidal waveforms for laser current modulation, as well as to trigger frame acquisition signals in the infrared camera from its digital I/O. The modulation frequency was set at 10 Hz. To acquire high signal-to-noise-ratio (SNR) lock-in in-phase and quadrature images, a 16× undersampling lock-in method was applied to the output image frames.

IV. RESULTS AND DISCUSSION

Equation (21) gives the LIC signal, $S_{CG}(\omega_M)$, in the one-dimensional carrier-density-wave approximation as a function of the radiative recombination efficiency. The proportionality constants C and K link the NIR detector/camera signal to the radiative emission process and can be consolidated as follows:[9]

$$S(\omega) \approx F(\lambda_1, \lambda_2)\int_0^L \Delta N^{\nu}(z,\omega)dz, \quad (35)$$

where the subscripts of S_{CG} and ω_M are henceforth dropped for simplicity. F is a function of the spectral bandwidth (λ_1, λ_2) of the IR detector/camera and of the excess electron and hole carrier densities $\Delta N(z,\omega)\Delta P(z,\omega)$. Under nearly intrinsic photocarrier transport conditions, this implies a quadratic dependence of the excess photocarrier density integrand ($\nu = 2$).[24] The expected quadratic dependence is usually expressed as $B_{rad}\,\Delta N(z,\omega)\,[\Delta N(z,\omega) + N_D]$ as shown in Eq. (33), where N_D is the doping density. Under low injection conditions, however, the linear dependence on $\Delta N(z,\omega)$ dominates[9,25] and the CG signals can be simplified with $\nu = 1$ which allows the integral in Eq. (35) to be calculated analytically.[9] In many PCR situations, the focused laser beam leads to intermediate injection conditions, or to

Downloaded 24 Sep 2013 to 128.100.48.8. This article is copyrighted as indicated in the abstract. Reuse of AIP content is subject to the terms at: http://jap.aip.org/about/rights_and_permissions

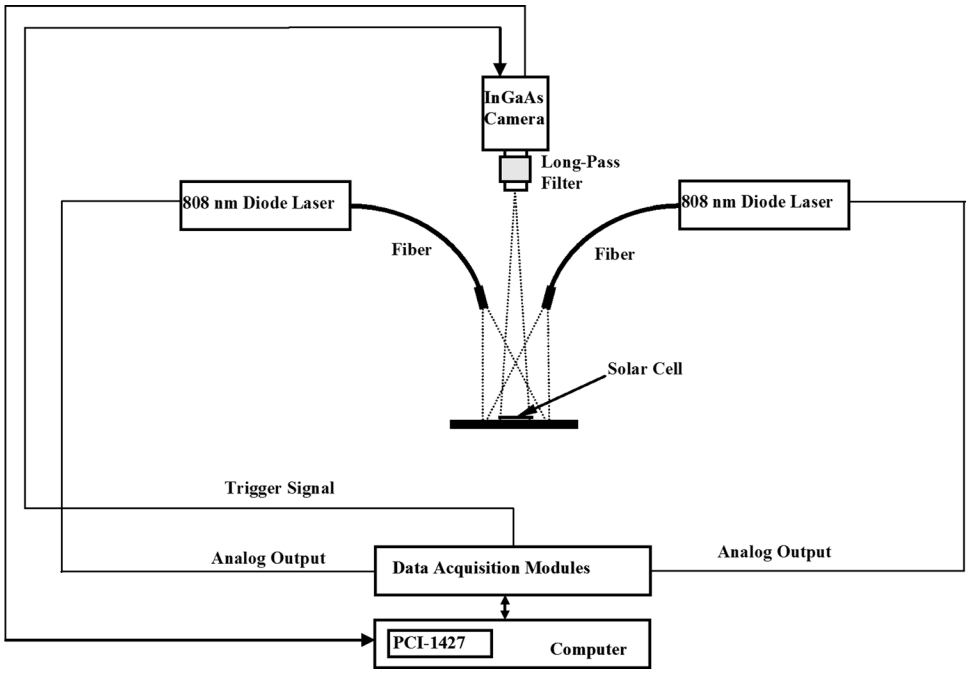

FIG. 1. LIC experimental set-up.

recombination of free carriers not involving the conduction and valence bands (e.g., from band-to-impurity or band-to-defect), both of which can be modeled with ν between 1 and 2.[21]

As discussed in Sec. II, in addition to bulk-averaged recombination lifetimes which characterize dc PL image contrast, the spatial (lateral as well as depth) resolution and contrast of LIC images is due to variations in modulated carrier-density-wave (CDW) amplitude and phase which are controlled by the ac carrier diffusion length and its dependence on the *local* band-to-band and (or) band-to-defect decay lifetime τ within the diffusion length. Other transport properties generic to semiconductor optoelectronics[21] or to specific solar cell parameters (shunt resistance, series and load resistances, junction capacitance)[16] also contribute to contrast.

A. Solar-cell LIC image pixel brightness distributions

The ten industrial solar cells labeled #1 to #10 were used for LIC measurements at room temperature at open circuit. CG amplitude and phase images of #8 are shown in Fig. 2, in which the metal electrodes on the front surface of the sample appear as two vertical strips. Figure 2(a) shows contrast due to a highly inhomogeneous distribution of radiative recombination processes across the solar cell, at the junction and mainly in the base of solar cell. The phase contrast in Fig. 2(b) is controlled by $L_e(\omega)$, Eq. (27), and is due to the phase lag contributed by depth variations of the CDW centroid[22] below the surface a function of the recombination lifetime τ, and/or by the non-linearity exponent ν.

Statistical histograms (camera pixel modulated brightness intensity distributions) over fully illuminated surfaces were obtained from all LIC images for the purpose of validating the theory of Sec. II with respect to quantitative dependencies of image pixel averages on solar conversion efficiency and photovoltage. The histograms show the number of pixels with amplitude (or phase) values within a range x and $x + \Delta x$ (Δx: "bin size"). The number of pixels in Δx is proportional to the corresponding area of the solar cell so it describes the fraction of the solar cell surface with signal values within the given range. Figure 3 shows a (typical) pair of LIC amplitude and phase histogram obtained from solar cell #8 using the images of Figs. 2(a) and 2(b), respectively. The amplitude image histogram at 10 Hz is broadly peaked at approximately 100 (arbitrary units). The narrow amplitude peak at, or near, zero is due to very low pixel

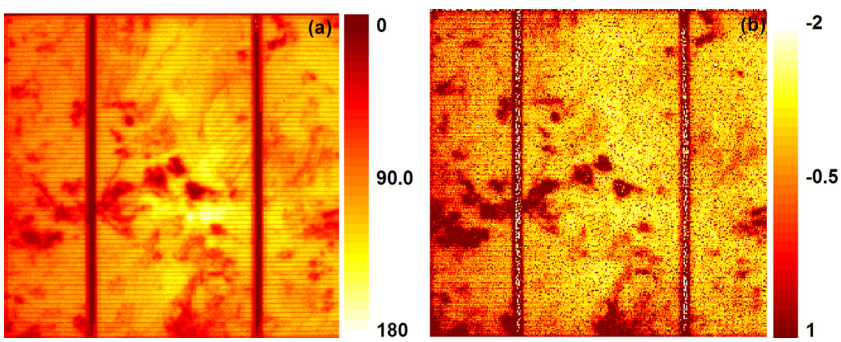

FIG. 2. LIC of whole solar cell #8 at 10 Hz: (a) amplitude and (b) phase image.

Downloaded 24 Sep 2013 to 128.100.48.8. This article is copyrighted as indicated in the abstract. Reuse of AIP content is subject to the terms at: http://jap.aip.org/about/rights_and_permissions

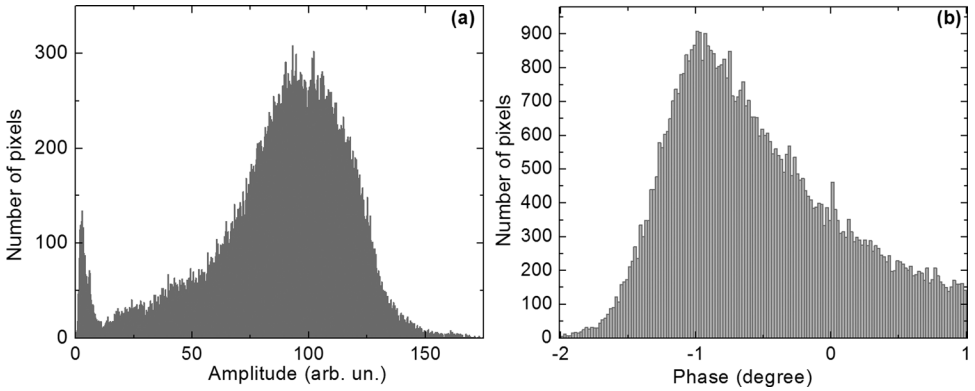

FIG. 3. Statistical pixel brightness distributions of LIC image (a) amplitude with bin size 0.25 and (b) phase with bin size 0.02 (b) of solar cell #8 obtained at 10 Hz.

readings contributed from regions on, or near, the electrodes. The longer tail on the left side of the amplitude histogram and on the right side of the phase is associated with contributions from solar cell areas with very low LIC amplitude. The phase image histogram is peaked at ca. -1°. It should be mentioned that a phase lag at 10 Hz is very small with high level of noise especially in short lifetime regions. The small contrast of the phase image in this case is used for demonstrating trends in phase behavior and for correlating them to amplitude trends. It is also used to validate the predictions of the theoretical model. As was shown earlier,[16] the highest contrast in LIC amplitude and phase images is at frequencies corresponding to the recombination lifetime ($2\pi f \sim 1/\tau$).

The statistical results of the LIC image pixel modulated brightness distributions from all ten solar cells obtained at 10 Hz are shown in Table I. To calculate their solar conversion efficiencies and other electrical parameters, a load resistance box was used to measure the I-V characteristics with dc illumination provided by the two 808-nm diode lasers. The current I through the load resistance R_L and the voltage V across R_L were measured by changing the value of the resistive load. The experimental I-V characteristics of a solar cell were fitted to Eq. (11) in the form $I(V) = J(V)S$ (S: solar cell surface area) which, however, does not take into account the series resistance in the solar cell. The values of J_{SC}, J_0, n, and R_{sh} were thus calculated for all cells. As an example, the I-V characteristics of solar cell #8 and the theoretical best fit are shown in Fig. 4. The maximum power, $P_M = V_{mp}I_{mp}$ (mW), was calculated from the voltage and current at the maximum power point. Using the experimental P_M values, the solar conversion efficiency was obtained from[26]

$$\eta = \frac{P_M}{J_i \times S} \times 100\%, \tag{36}$$

where J_i is incident light irradiance (mW/cm^2) and S is the surface area of the solar cell (cm^2). The calculated results in Table I show that the efficiencies of the ten solar cells ranged from 16.6% to 17.7%, values which are in agreement with those provided by the manufacturer. The table also includes the best-fitted values of the other electrical parameters of the solar cells, as well as the LIC results of the pixel histogram statistics. The parameter "Sum" is the sum of the amplitudes of all the pixels (excluding the pixels of the vertical dark strips corresponding to the front surface metal electrodes) divided by the area of the solar cell illuminated in the amplitude images. The parameter "Max" is the distribution of phase maxima. These are essentially numerical integrals of the distributions in Fig. 3 and correspond to the amplitude average of Eq. (23) and a similar one for the mean phase surface integral implied in Eq. (30).

B. Surface-averaged η dependence on LIC image pixel brightness distribution

The dependence of solar conversion efficiency and photovoltage on the full-surface pixel brightness statistical

TABLE I. Electrical and LIC statistical parameters of the 10 solar cells.

	Electrical parameters ($J_i = 20.5$ mW/cm^2)					Surface averaged LIC amplitude	LIC phase
Name of solar cell	J_{sc} (mA/cm^2)	J_0 (nA/cm^2)	n	η (%)	P$_m$/S (mW/cm^2)	Sum (arb.un/cm^2)	Max (degree)
#1	7.85	1.550	1.41	16.6	3.398	21.2×10^3	−0.79
#2	8.04	1.709	1.42	17.1	3.497	27.3×10^3	−0.55
#3	7.91	1.583	1.41	16.6	3.411	21.2×10^3	−0.61
#4	7.91	1.914	1.43	16.6	3.416	20.9×10^3	−0.87
#5	7.92	1.511	1.41	16.8	3.44	20.1×10^3	−0.68
#6	7.88	1.224	1.39	16.8	3.437	21.3×10^3	−0.9
#7	7.93	1.109	1.38	16.9	3.466	25.1×10^3	−0.93
#8	8.09	1.74	1.42	17.2	3.519	24×10^3	−0.96
#9	8.36	1.76	1.41	17.7	3.63	31.5×10^3	−0.97
#10	8.2	1.68	1.38	17.4	3.56	23.8×10^3	−0.68

Downloaded 24 Sep 2013 to 128.100.48.8. This article is copyrighted as indicated in the abstract. Reuse of AIP content is subject to the terms at: http://jap.aip.org/about/rights_and_permissions

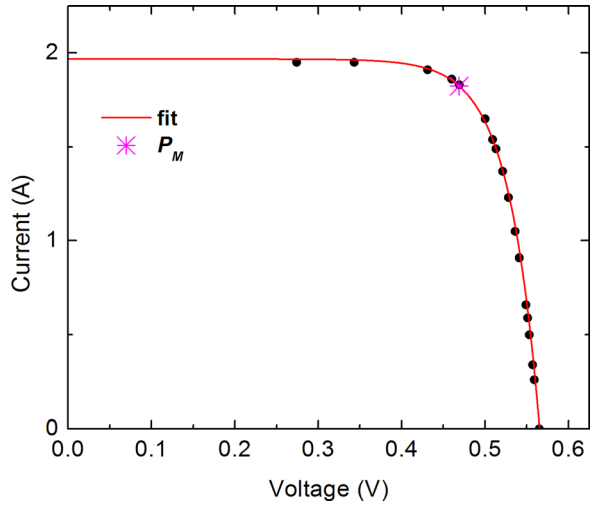

FIG. 4. I-V characteristics of solar cell #8. Best-fit values $J_{SC} = 8.096$ mA/cm^2, $J_o = 1.74$ nA/cm^2, $n = 1.42$, $R_{sh} = 1000$ Ω, $\chi^2 = 0.00027$, and $R^2 = 0.99945$ denote an excellent fit of Eq. (11) to the data.

average was obtained for all solar cells under investigation, as the non-contacting lock-in carrierographic equivalent of the conventional electrical measurements averaged over a fully electroded solar cell surface. In view of Eqs. (26) and (30), the plots of Fig. 5 were obtained in which solar conversion efficiencies are shown to be proportional to the Sum (logarithms) of the 10-Hz LIC amplitude images. The efficiencies are also seen to be linearly dependent on Max (phases). These results are in agreement with Eqs. (26) and (30), respectively. The best fits to straight lines shown in Fig. 5 yielded slopes and intercepts indicated in the caption of Fig. 5. Given the instrumentally unnormalized nature of the carrierographic amplitude (constant C in Eq. (26)), both slope and intercept must be calibrated through a multiplicative constant, in order to reflect accurate values of the groupings of parameters involved. It should be noted that, with typical Si solar-cell lifetimes τ normally ≤ 1 ms, at 10 Hz, Eq. (27) becomes $L_e(\omega) \approx \sqrt{D^*\tau}$. Therefore, the ac carrier diffusion length is equal to the dc carrier diffusion length which makes the LIC amplitude images exhibit the same features as their dc counterpart PL images. However, LIC produces phase images as a second independent imaging channel, while the dark current in the camera pixels as well as noise and dc background are strongly suppressed in the lock-in method. The experimental results of Fig. 5(a) and additional PCR signal frequency measurements at several locations across the surface of the solar cells (not shown here) follow the general trends: Larger mean-value sum (amplitudes) corresponds to higher solar conversion efficiencies and longer recombination lifetimes, as expected intuitively and concretely from the η proportionality to ΔJ, Eq. (16), with $\Delta J \equiv J_{SC} - J_{NR}$. High-optoelectronic-quality solar cells exhibit minimum J_{NR} which maximizes η. Shorter recombination lifetime leads to smaller phase lag and is commensurate with smaller conversion efficiency η, as observed in Fig. 5(b).

C. LIC image pixel brightness distribution dependence on surface damage

To further investigate the applicability of the results of the statistical methodology theory to the non-contacting study of the solar conversion efficiency dependence on other device parameters shown in Eq. (10) and its electrical counterpart, Eq. (11), solar cell #2 was selected and sequentially front-surface-damaged 3 times through rubbing with fine sandpaper, followed by LIC imaging at 10 Hz. Moreover, electrical measurements followed: the shunt resistance, R_{sh}, of the solar cell was also measured before and after each rubbing procedure. It was found that without damage, R_{sh} was 23.5 kΩ. After rubbing it changed to 0.80, 0.34, and 0.31 kΩ sequentially. The LIC pixel brightness amplitude distributions representing the rubbed area significantly shifted to lower values after the first rubbing and beyond. The results of mechanical damage are shown in Figs. 6(b)–6(d). The pixel phase distributions also shifted to decreasing values (smaller lags) owing to the shortened effective recombination lifetime after mechanical damage, Fig. 7.

The R_{sh} decreases recorded after each rubbing procedure are equivalent to increasing non-radiative current density (energy decay pathways) in the sense of both corresponding to wasted energy, as follows from the comparison of

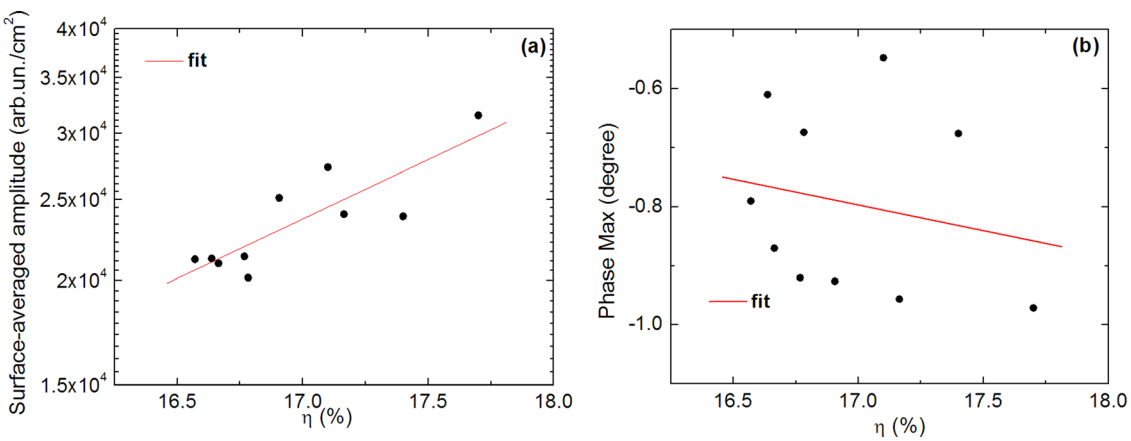

FIG. 5. Dependence of surface-averaged 10-Hz lock-in carrierographic amplitude (a) and phase maximum distribution (b) on the efficiency for 10 solar cells. Best-fit slopes and intercepts are amplitude 0.14 and 91, phase −0.087° and 0.68°, respectively. Illumination power density: 0.041 W/cm^2.

Downloaded 24 Sep 2013 to 128.100.48.8. This article is copyrighted as indicated in the abstract. Reuse of AIP content is subject to the terms at: http://jap.aip.org/about/rights_and_permissions

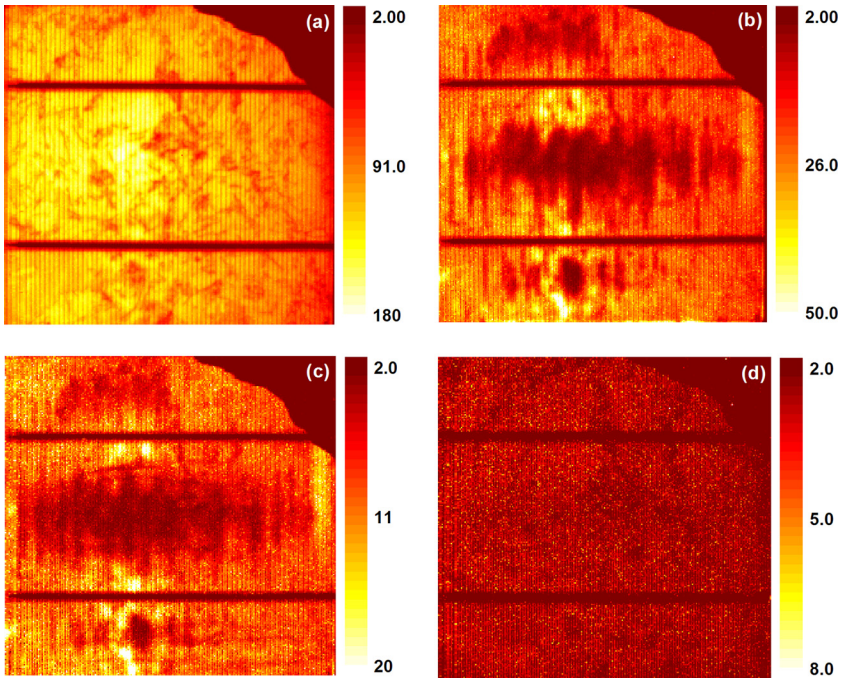

FIG. 6. LIC amplitude images of solar cell #2 before (a) and after (b)-(d) three rubbings with fine sandpaper imparting near-surface mechanical damage. Note the monotonic amplitude distribution decreases.

Eqs. (10) and (11). The worst damaged images, Figs. 6(d) and 7(d), show that the decrease in radiative recombination events across the surface severely impacted image contrast. The large amplitude decreases due to the shift in recombination mechanism to non-radiative, induced the deteriorated image quality in both amplitude and phase channels. The contrast became so low that the damaged areas could not be distinguished from the intact parts of the surface while both regions exhibited compromised signal quality. This interesting lateral interaction effect may be due to the lateral diffusion and redistribution of photoexcited carriers: In isotropic high quality semiconductors, large local carrier-wave densities diffuse spherically around their generation spot, and in doing so, they highlight contrast with neighboring low-quality regions, e.g., through rapid non-radiative decay mechanisms. As the high-quality locations become damaged, this lateral charge transfer decreases and ultimately ceases, resulting in poor or non-existent radiative recombination contrast even in the non-damaged regions.

For quantitative purposes, statistical pixel brightness distribution histograms were also constructed for all LIC amplitude and phase images shown in Figs. 6 and 7. The results are shown in Figs. 8 and 9, respectively. The amplitude histogram of solar cell #2 before damage is similar to that of

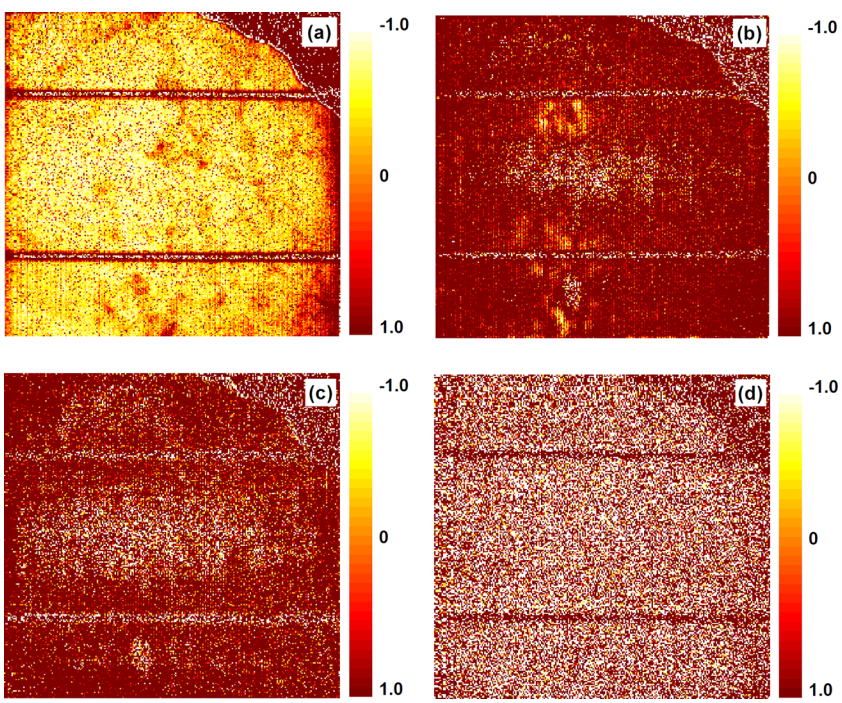

FIG. 7. LIC phase images of solar cell #2 before (a) and after (b)-(d) three rubbings with fine sandpaper imparting near-surface mechanical damage.

Downloaded 24 Sep 2013 to 128.100.48.8. This article is copyrighted as indicated in the abstract. Reuse of AIP content is subject to the terms at: http://jap.aip.org/about/rights_and_permissions

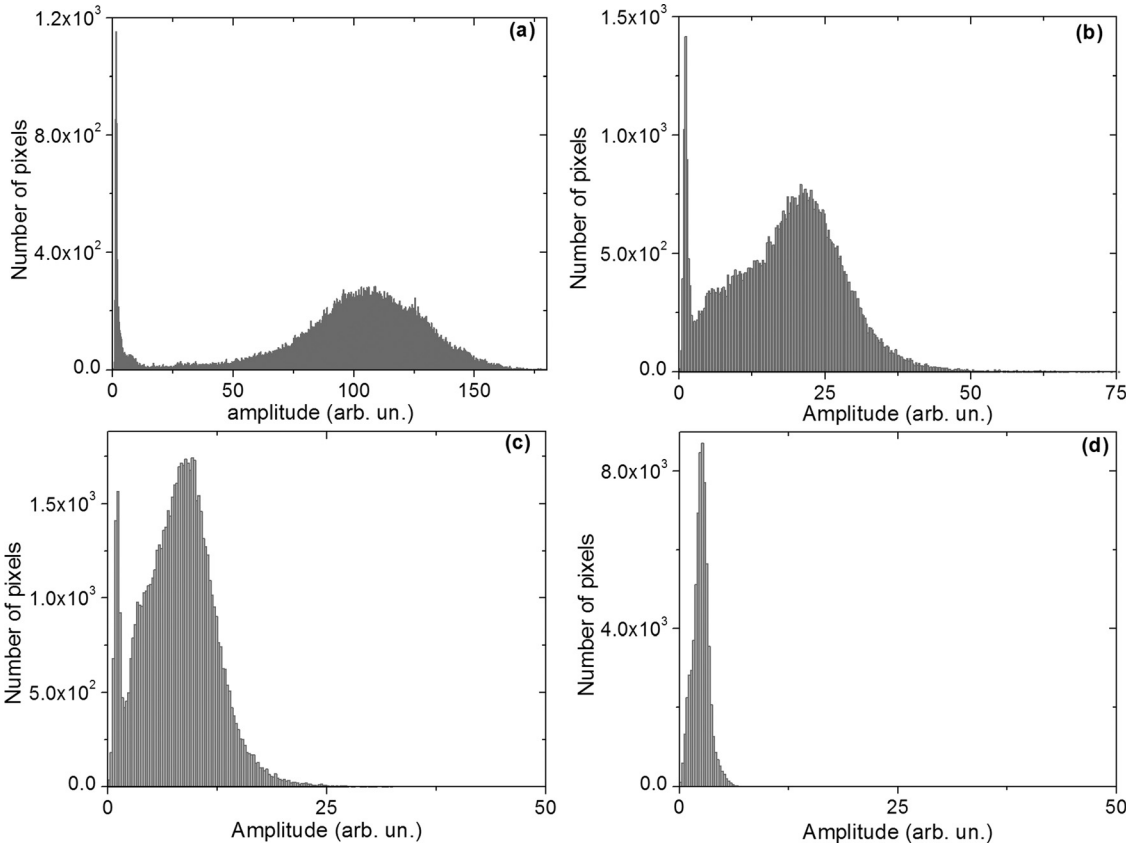

FIG. 8. Statistical pixel brightness distributions of the amplitudes of the LIC images shown in Fig. 6. (a)–(d) correspond to (a)–(d) images of that figure, respectively. Bin size = 0.25.

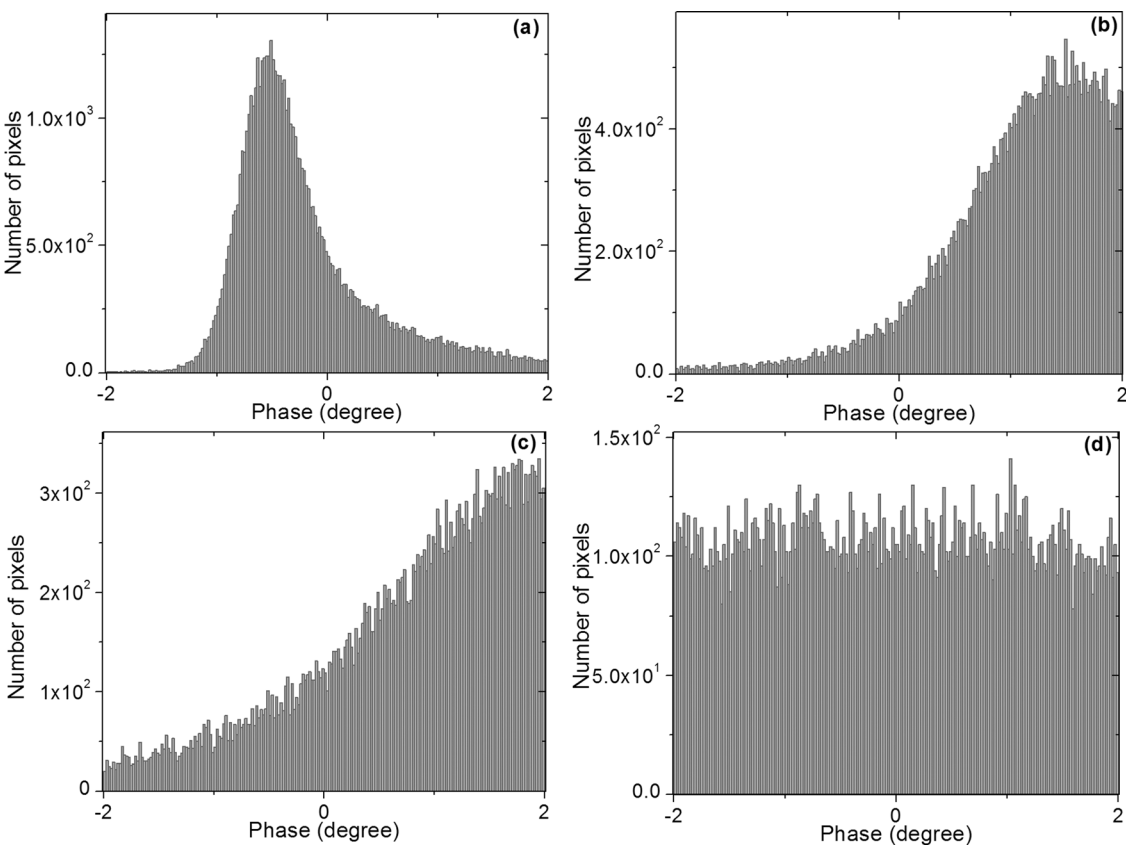

FIG. 9. Statistical pixel brightness distributions of the phases of the LIC images shown in Fig. 7. (a)–(d) correspond to (a)–(d) images of that figure, respectively. Bin size = 0.02.

Downloaded 24 Sep 2013 to 128.100.48.8. This article is copyrighted as indicated in the abstract. Reuse of AIP content is subject to the terms at: http://jap.aip.org/about/rights_and_permissions

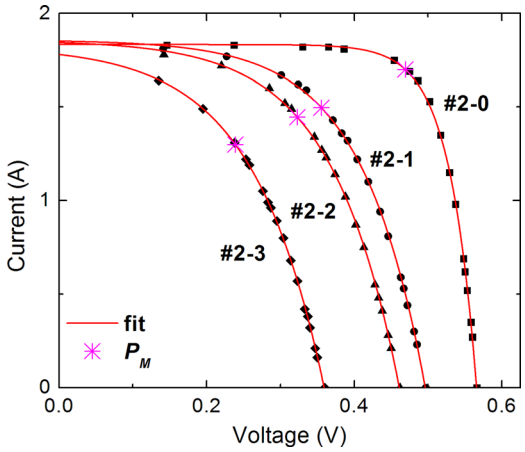

FIG. 10. I-V characteristics of solar cell #2. S = 228 cm^2.

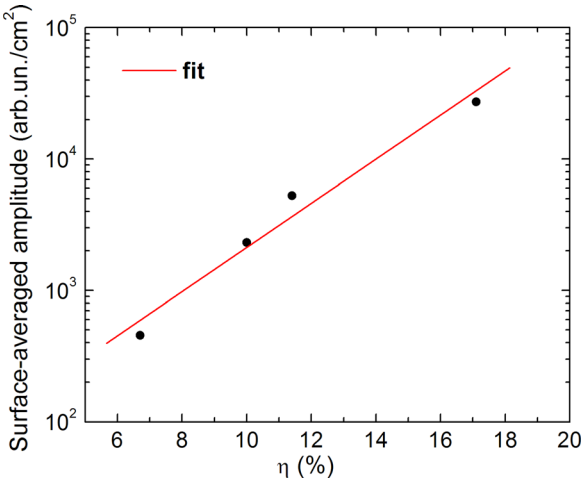

FIG. 11. Dependence of surface-averaged 10-Hz lock-in carrierographic amplitude on the conversion efficiency for surface damaged solar cell #2. Best-fit slope and intercept are 0.17 and 44. Illumination power density: 0.041 W/cm^2.

#8, Fig. 3(a), except for a much higher peak of the left, which was contributed by a broken corner. The phase-image histogram also shows similarities to Fig. 3(b). After the first and second rubbings, with the exception of the near-zero contributions of the electrode and the broken corner, the main peak in the amplitude image significantly shifted to the left with the peak growing narrower and taller because the total pixel number remained fixed. After the third rubbing, the main peak in the amplitude image entirely overlapped the leftmost peak corresponding to the electrodes and the broken corner. The narrowness of this peak is a statistical manifestation of the fully deteriorated image contrast. On the contrary, in the pixel phase distribution, Fig. 9, the main peak shifted to the right in agreement with the imaging trends of Fig. 7.

Using the method of Sec. IV A, the solar conversion efficiency and other parameters of solar cell #2 were obtained, including the maximum power before and after mechanical damage. The *I-V* characteristics are shown in Fig. 10. The best fits to Eq. (11) are excellent for all stages of mechanical damage and the calculated parameters are shown in Table II. Figure 11 is similar to Fig. 5, however, the plots show smaller scatter, thereby better validating the statistical theory of Sec. II, specifically Eqs. (26).

D. LIC image pixel brightness distribution dependence on photovoltage (load resistance)

According to the theoretical expression (34), the closed- and open-circuit mean photovoltage is expected to have a logarithmic relationship to the surface-integrated LIC image pixel amplitude distribution. One solar cell was irradiated uniformly with laser intensity 0.04 W/cm^2. The statistical distribution peak under smaller load resistance, Fig. 12, shifted toward decreasing radiative recombination amplitudes with decreasing photovoltage, with a concomitant reduction of the half-width of the distribution. As with the measurements reported in Secs. IV A–IV C, it should be mentioned that owing to the surface metallic grid, the local photovoltage can be assumed constant over the surface of the investigated solar cell under small illumination intensity (0.04 W/cm^2). The presence of the grid minimizes or eliminates areas of high series resistance and leads to out-diffusion of excess minority carriers from areas with long recombination lifetime (high carrier-wave density) to areas with short lifetime (low density), as well as to shunt resistance (non-radiative recombinations) under open circuit conditions. As a result, PL from areas with long carrier lifetime significantly decreases and the surface-integrated CG amplitude reflects terminal voltage as well as average transport parameters that determine the generation current across the entire solar cell. Figure 13 clearly confirms experimentally the theoretical prediction of Eq. (34) and its open-circuit special case, Eq. (32), whose mean value is written in the form

$$\langle \ln(CS_{CG}) \rangle = \left\langle \left(\frac{qP_i}{nkT\Delta J} \right) \right\rangle \langle V_{\hbar\omega} \rangle - \left\langle \ln\left(\frac{\Delta J - J}{qF_R(0)} \right) \right\rangle. \tag{37}$$

TABLE II. Electrical and LIC statistical parameters of solar cell #2 with mechanical damage.

Solar cell # vs. mechanical damage round	Electrical parameters (J_i = 20.5 mW/cm^2)					Surface averaged LIC amplitude	LIC phase
	J_{sc} (mA/cm^2)	J_0 (nA/cm^2)	n	η (%)	P_m/S (mW/cm^2)	Sum (arb.un/cm^2)	Max (degree)
#2-0	8.04	1.71	1.42	17.1	3.5	27.3×10^3	−0.55
#2-1	8.12	25.2	3.32	11.4	2.33	5.28×10^3	1.5
#2-2	8.09	52.4	3.53	10	2.05	2.32×10^3	
#2-3	7.81	193	3.733	6.64	1.36	0.456×10^3	

Downloaded 24 Sep 2013 to 128.100.48.8. This article is copyrighted as indicated in the abstract. Reuse of AIP content is subject to the terms at: http://jap.aip.org/about/rights_and_permissions

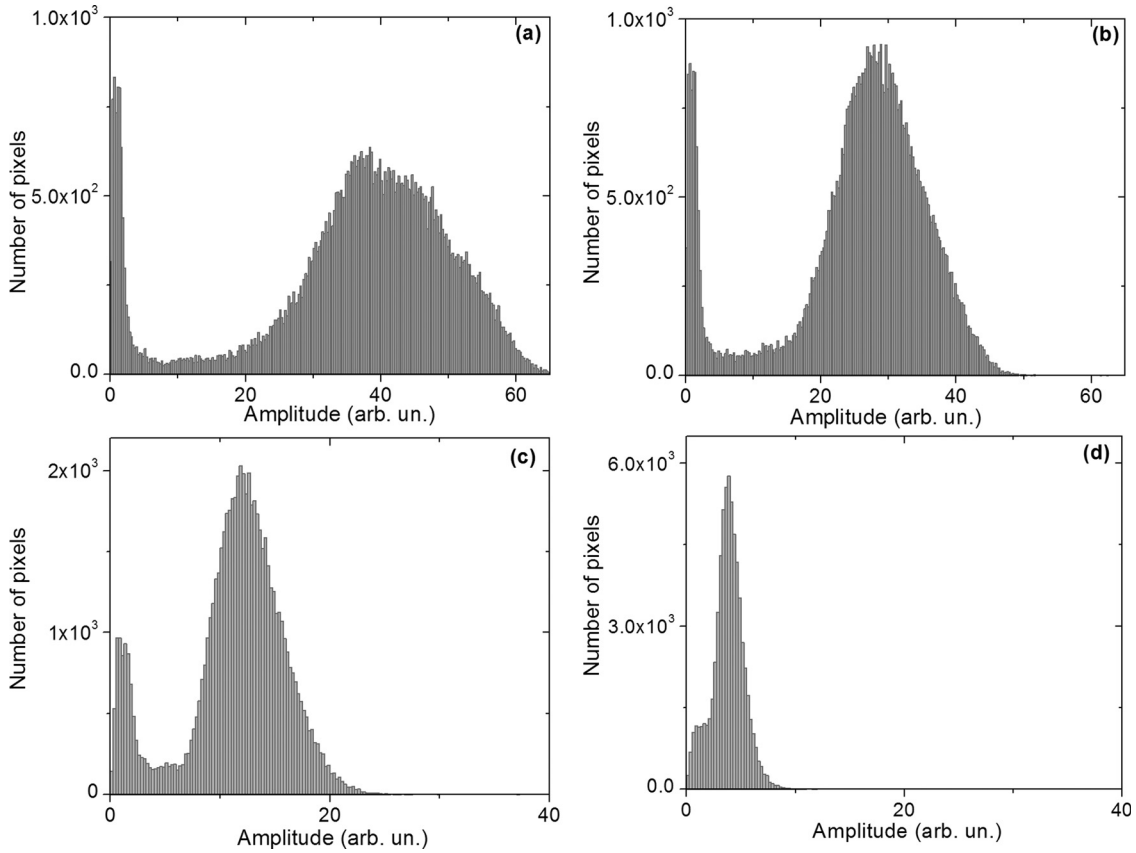

FIG. 12. Statistical pixel brightness distributions of LIC images amplitudes shown in the inset of Fig. 13 for photovoltage 581 mV (a), 566 mV (b), 539 mV (c), and 505 mV (d). Photovoltage was varied as a function of load resistance and was measured at maximum laser power. Bin size = 0.25.

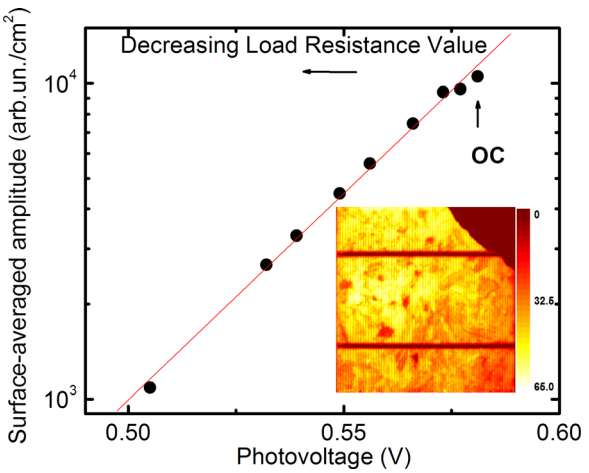

FIG. 13. Surface-integrated 10-Hz LIC amplitude dependence on terminal photovoltage. Photovoltage was varied as a function of load resistance and was measured at maximum laser power. Best-fit slope and intercept are 13.1 and 0, respectively. Illumination power density: 0.04 W/cm^2.

V. CONCLUSIONS

A theoretical solid state formalism for the dependence of the photocarrier radiometric and/or lock-in carrierographic imaging signal on optoelectronic properties of solar cells was developed and was shown to result in a simple analytical relationship between the emitted radiative recombination photon flux (current density) and the major output characteristic parameters of solar cells, namely the solar conversion efficiency and the closed- and open-circuit photovoltage. It was shown that the relationship between carrierographic signal and solar cell parameters is based on the similarity of the conventional diode equation (11) and the new optoelectronic equation (10). This similarity allows the non-contacting image-based measurement of several key parameters of the full-surface illuminated solar cell with pixel brightness acting as a statistically averaging radiative-emission distribution network over the surface, much like contacting electrical measurements make use of the outputs of the surface-distributed electrode grid. The major parameters are the closed- and open-circuit photovoltage and the solar conversion efficiency. The theory was extended to measure mean values of these important parameters. The statistical theory was confirmed using multi-crystalline Si solar cells and illumination at 10 Hz modulation frequency.

ACKNOWLEDGMENTS

The authors are grateful to Enfoton Solar, Kokkinotrmithia, Cyprus, for supplying the solar cells for this research. A.M. is grateful to NSERC for a Discovery grant, to the Canada Foundation for Innovation (CFI) for equipment grants, to the Canada Research Chairs Program, and to the Ontario Ministry for Research and Innovation (MRI) for the Inaugural Premier's Discovery Award in Science and Technology (2007).

Downloaded 24 Sep 2013 to 128.100.48.8. This article is copyrighted as indicated in the abstract. Reuse of AIP content is subject to the terms at: http://jap.aip.org/about/rights_and_permissions

[1]I. Latchford and J. B. True, Photovoltaics World, Issue 4, July/August 2011.
[2]M. Bail, M. Schulz, and R. Brendel, Appl. Phys. Lett. **82**, 757 (2003).
[3]J. Schmidt and A. G. Aberle, J. Appl. Phys. **81**, 6186 (1997).
[4]W. M. Keogh, A. W. Blakers, and A. Cuevas, Sol. Energy Mater. Sol. Cells **81**, 183 (2004).
[5]T. Trupke, R. A. Bardos, M. C. Schubert, and W. Warta, Appl. Phys. Lett. **89**, 044107 (2006).
[6]M. The, M. C. Schubert, and W. Warta, in *Proc. 22nd EUPVSEC* (2007), p. 354.
[7]D. Macdonald, J. Tan, and T. Trupke, J. Appl. Phys. **103**, 073710 (2008).
[8]J. Giesecke, M. Kasemann, and W. Warta, J. Appl. Phys. **106**, 014907 (2009).
[9]A. Mandelis, J. Batista, and D. Shaughnessy, Phys. Rev. B **67**, 205208 (2003).
[10]W. Shockley and H. J. Queisser, J. Appl. Phys. **32**, 510 (1961).
[11]A. Mandelis, Solid-State Electron. **42**, 1 (1998).
[12]J. Isenberg and W. Warta, Prog. Photovoltaics **12**, 339 (2004).
[13]O. Breitenstein M. Langenkamp, O. Lang, and A. Schirrmacher, Sol. Energy Mater. Sol. Cells **65**, 55 (2001).
[14]M. Kasemann, M. C. Schubert, M. The, M. Köber, M. Hermle, and W. Warta, Appl. Phys. Lett. **89**, 224102 (2006).
[15]J. Batista, A. Mandelis, and D. Shaughnessy, Appl. Phys. Lett. **82**, 4077 (2003).
[16]A. Melnikov, A. Mandelis, J. Tolev, P. Chen, and S. Huq, J. Appl. Phys. **107**, 114513 (2010); A. Melnikov, A. Mandelis, J. Tolev, and E. Loiudakis, J. Phys.: Conf. Ser. **214**, 012111 (2010).
[17]P. Würfel, J. Phys. C **15**, 3967 (1982).
[18]P. Würfel, S. Finkbeiner, and E. Daub, Appl. Phys. A **60**, 67 (1995).
[19]A. L. Fahrenbruch and R. H. Bube, *Fundamentals of Solar Cells* (Academic, New York, 1983).
[20]A. K. Ghosh, C. Fishman, and J. Teng, J. Appl. Phys. **51**, 446 (1980).
[21]J. Tolev, A. Mandelis, and M. Pawlak, J. Electrochem. Soc. **154**, H983 (2007).
[22]A. Mandelis, *Diffusion-Wave Fields: Mathematical Methods and Green Functions* (Springer-Verlag, New York, 2001), Chap. 9.
[23]T. Trupke, R. A. Bardos, M. D. Abbott, and J. E. Gotter, Appl. Phys. Lett. **87**, 093503 (2005).
[24]D. Guidotti, J. S. Batchelder, A. Finkel, P. D. Gerber, and J. A. Van Vechten, J. Appl. Phys. **66**, 2542 (1989).
[25]J. S. Blakemore, *Semiconductor Statistics* (Dover, Mineola, NY, 1987), Chap. 5.
[26]S. M. Sze, *Physics of Semiconductor Devices*, 2nd ed. (Wiley, New York, 1981), Chap. 14.

Downloaded 24 Sep 2013 to 128.100.48.8. This article is copyrighted as indicated in the abstract. Reuse of AIP content is subject to the terms at: http://jap.aip.org/about/rights_and_permissions